Scientific Research Publishing

Open Journal of Earthquake Research, 2024, 13, 27-40
https://www.scirp.org/journal/ojer
ISSN Online: 2169-9631
ISSN Print: 2169-9623

Fundamental Study on Response Properties of Structures Constructed on Lunar Regolith

Yuji Miyamoto[1], Takaharu Nakano[2], Toshio Kobayashi[3]

[1]Department of Architecture and Civil Engineering, Fukui University of Technology, Fukui, Japan
[2]Graduate School of Engineering, Osaka University, Osaka, Japan
[3]SANSEI, Inc., Tokyo, Japan
Email: miyamoto@fukui-ut.ac.jp

How to cite this paper: Miyamoto, Y., Nakano, T. and Kobayashi, T. (2024) Fundamental Study on Response Properties of Structures Constructed on Lunar Regolith. *Open Journal of Earthquake Research*, **13**, 27-40.
https://doi.org/10.4236/ojer.2024.131002

Received: January 7, 2024
Accepted: February 6, 2024
Published: February 9, 2024

Abstract

The Artemis Program, for constructing the lunar base, is in progress. How to design and construct architectural and civil engineering structures in the lunar environment has become an important issue. The lunar surface is covered with soft sand, called regolith, and it is required to protect lunar bases and structures, as well as internal precision equipment, against vibrational disturbances such as moonquakes and meteorite collisions. Therefore, in this study, the static and cyclic triaxial compression tests of the regolith simulant were conducted. The reference strain and equivalent damping factor of the regolith simulant were smaller compared to sandy soil on Earth. In addition, a shaking table test using model specimens was conducted on the response properties of regolith ground alone and structures set on regolith ground. The buried foundation and pile foundation notably suppressed the horizontal response attributed to the rocking component compared to a direct foundation.

Keywords

Lunar Development, Regolith, Soil-Structure Interaction, Triaxial Compression Test, Shaking Table Test

1. Introduction

1.1. Research Background and Purpose

More than half a century has passed since humanity's first manned voyage to the moon through the Apollo 11 Mission in 1969 [1]. Presently, the U.S. National Aeronautics and Space Administration (NASA) is championing a manned space exploration endeavor aimed at establishing a lunar base (the Artemis Program) [2]. Concurrently, Japan's National Aerospace Exploration Agency (JAXA) is ac-

tively involved in this project, with private construction industries exploring potential opportunities in space-related businesses [3]. Given these circumstances, accumulating fundamental data pertaining to the design of various structures essential in a lunar setting becomes imperative. These structures will serve as exploration bases for humankind to commence lunar activities, eventually leading to the construction of lunar cities, social infrastructure, and underground structures, as shown in Figure 1.

As illustrated in Figure 2, the design of lunar structures must account for the

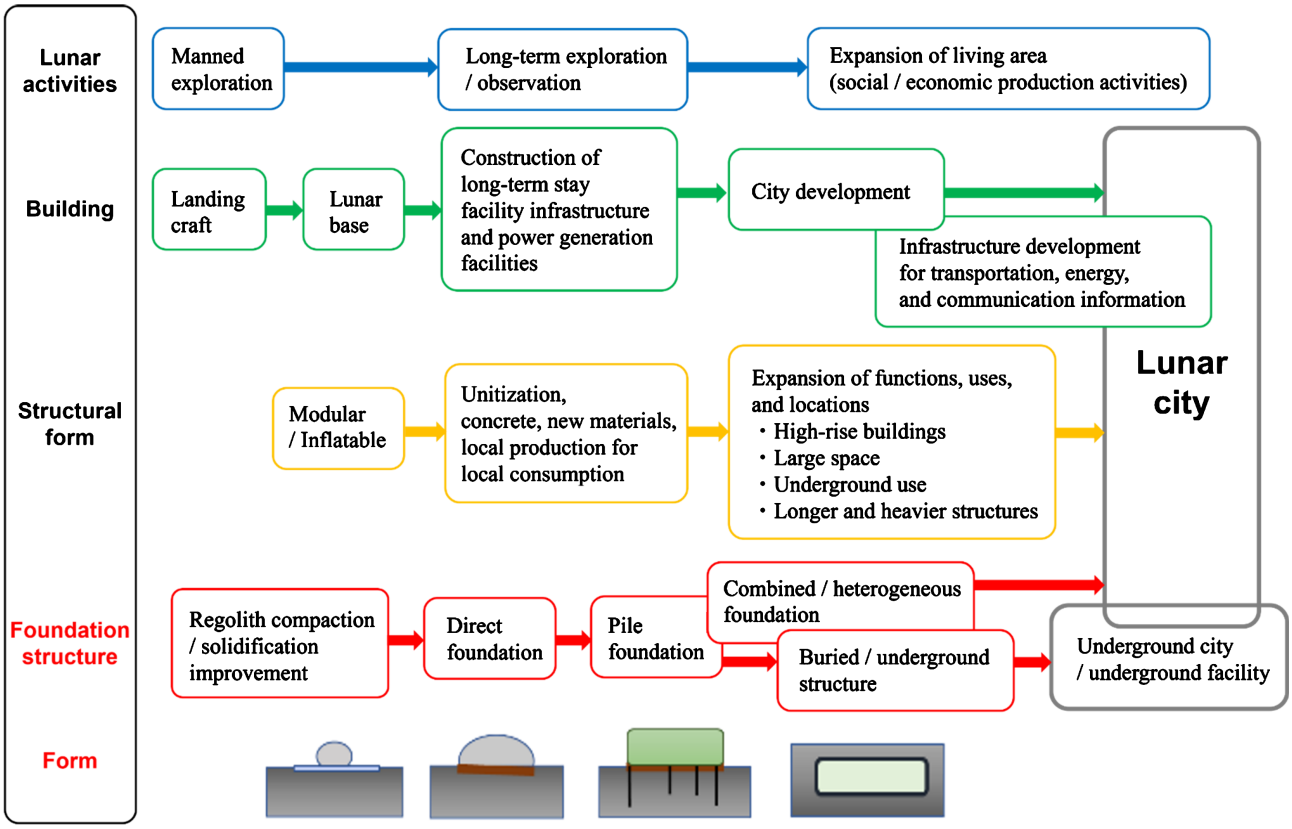

Figure 1. Prediction of changes in structural form of buildings and foundations with progressive lunar activities.

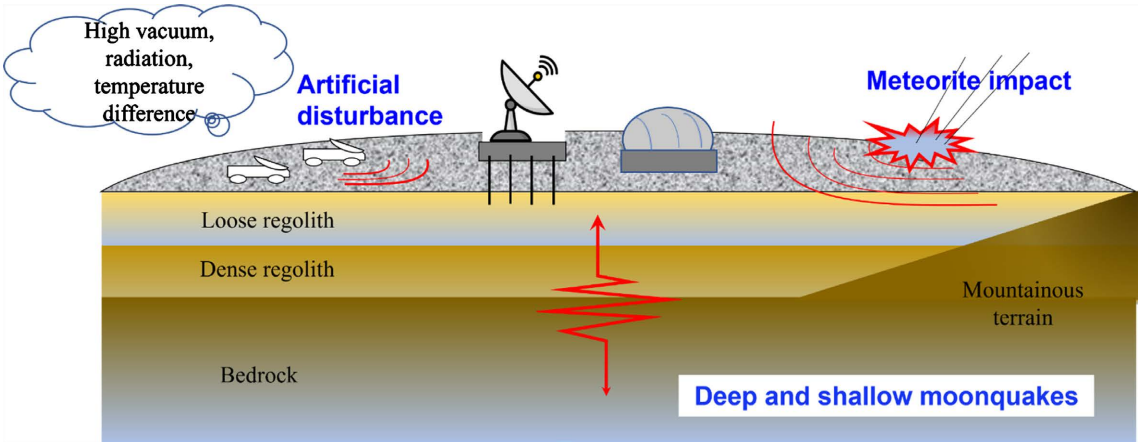

Figure 2. Schematic diagram of lunar structures and vibration disturbances.

lunar surface's coverage by soft sand (regolith). These structures necessitate the capability to securely support and sustain exploration bases, structures, and important equipment such as communication antennas in response to moonquakes, lunar surface tremors caused by meteorite impacts, and vibrations disturbances such as the movement of lunar rovers due to human activities. However, while research utilizing regolith simulants is currently limited [4] [5], knowledge regarding soil properties and foundational engineering specific to regolith that supports buildings remains scant. Additionally, almost no studies focus on the dynamic behavior of regolith and its interactions with foundations. Therefore, the objective of the present study is to conduct soil tests using regolith simulants and shaking table experiments to amass essential data concerning the response properties of lunar structures.

1.2. Previous Knowledge Regarding Lunar Regolith and Vibration Disturbance

1.2.1. Lunar Regolith

The bright regions of the lunar surface (highlands) predominantly consist of plagioclase, while the dark regions (seas) are primarily composed of basalt [6]. Erosion is absent on the lunar surface, and there is no observed plate movement or volcanic activity. However, factors like solar heat, electromagnetic waves from various sources, and meteorite impacts gradually weather the surface rocks over hundreds of millions of years, transforming the rock into soil rich in fine particles known as regolith.

Samples of regolith retrieved by the Apollo Missions have been brought back to Earth for analysis of their composition and mechanical properties [7]. Regolith exhibits distinctive features such as irregularly shaped soil particles due to the absence of atmospheric or water-induced weathering and a substantial amount of glass, believed to be a byproduct of meteorite impacts [8]. Institutions worldwide have developed simulants aimed at replicating the Apollo Mission samples [8], and for this study, we utilized the regolith simulant "FJS-1" [9]. **Figure 3** illustrates the results of the particle size test, indicating that approximately 44% of the sample's mass passes through a 75-μm diameter sieve, signifying

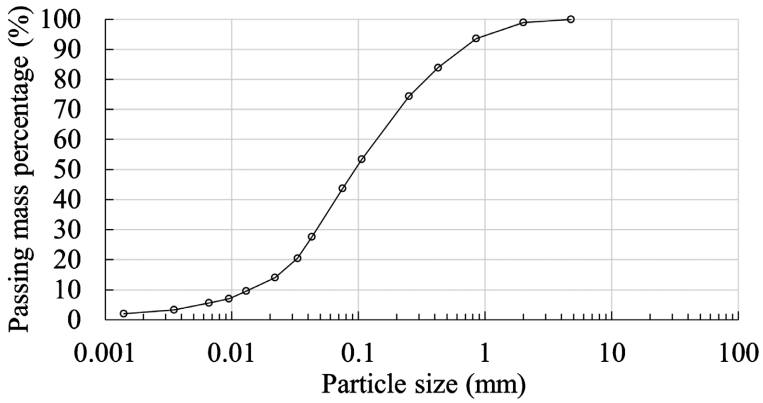

Figure 3. Particle size test results for regolith simulant "FJS-1".

the abundance of fine particles within the sample.

1.2.2. Vibration Disturbance

Observational data obtained from seismometers deployed during the Apollo Missions revealed the occurrence of moonquakes on the Moon, albeit less frequent compared to those on Earth [10]. These quakes are categorized as deep moonquakes, shallow moonquakes, thermal moonquakes, and meteorite-induced tremors. Causes attributed to moonquakes encompass tidal forces resulting from Earth's gravity and temperature fluctuations due to sunlight [11]. The energy released during moonquakes is estimated to be equivalent to M 0.5 - 1.3 for deep quakes [11] and M 4 - 5 for shallow ones [12]. Moonquake records have been used primarily to estimate the moon's internal structure [13] [14]. Moonquake durations typically exceed those of earthquakes, with a stronger influence of scattering [13] [14]. A predominant waveform component around 1 Hz has been identified [15]. Over a seven-year period, it has been reported that approximately 15% of observed waves were triggered by meteorite impacts, totaling 1743 instances [14]. Additionally, artificial disturbances stemming from human activities such as the movement of lunar rovers are predicted to occur.

1.3. Experimental Design and Specimens

In this study, preliminary static and cyclic triaxial compression tests were conducted to elucidate the mechanical properties of the regolith simulant. Subsequently, shaking table tests were carried out on specimens featuring the regolith simulant alone, as well as specimens incorporating pile, direct, or buried foundations atop the regolith simulant, aiming to gauge both the regolith and foundation response properties. Among these, the buried foundation presents an application potential for harsh lunar environments characterized by radiation and temperature fluctuations. Additionally, subterranean spaces could serve as protective measures against meteorite collisions. Therefore, our investigation also targeted the response properties of underground structures.

Figure 4 and Figure 5 present a cross-sectional view and a photograph of the specimen, respectively. The shaking table employed in the experimentation was a miniature setup from Osaka University.

1) Ground: The regolith simulant "FJS-1" was distributed within a soil container using a shovel, followed by compaction. The ground had a thickness of 360 mm and maintained an average density of 1.90 g/cm^3 (equivalent to a relative density of 84%).

2) Specimen model: The specimen comprised a rigid steel body measuring 120 mm × 120 mm × 50 mm, weighing approximately 5.4 kg. For the pile foundation, round acrylic rods with an 8 mm diameter and a conical tip, each 100 mm in length, were affixed to the four corners using adhesive, as depicted in Figure 5(a). The pile heads extended about 5 mm above the ground surface, ensuring no contact between the specimen bottom and the ground. In the case of the direct foundation, sandpaper was affixed to the specimen bottom and set on

the ground surface. For the buried foundation, the foundation was buried 50 mm, aligning the specimen's top surface with the ground level.

3) Input wave: White noise comprising components below 50 Hz, lasting approximately 40 s, was utilized as the input wave, with the amplitude varying across five stages and fed into the shaking table.

4) Scaling law: Gravity on the lunar surface equates to approximately 1/6th times that of Earth. Therefore, this experiment conducted on Earth under 1 g conditions, employing the same scaling law [16] as observed in the centrifugal loading experiment results in Table 1. Therefore, on the lunar surface, the ground thickness is scaled to approximately 2 m, with the acceleration and vibration frequency reduced by a factor of 1/6. Table 2 presents a comparison between the maximum input acceleration during the experiment and the lunar surface value.

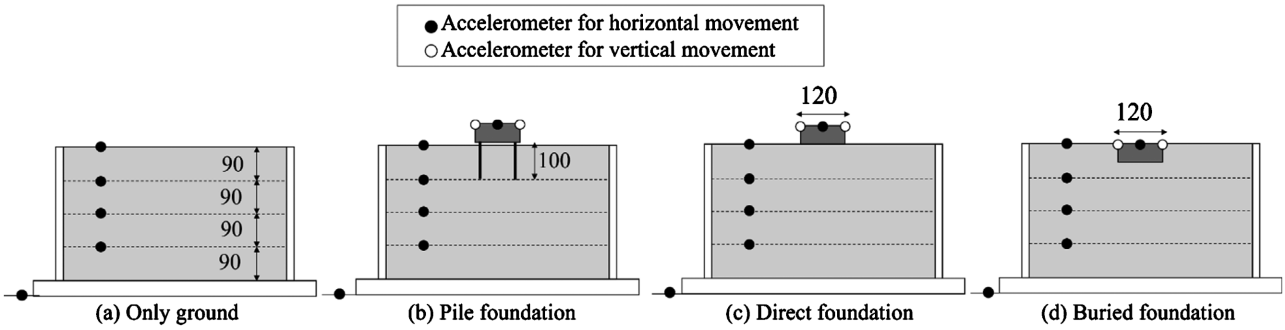

Figure 4. Cross-section of shaking table test.

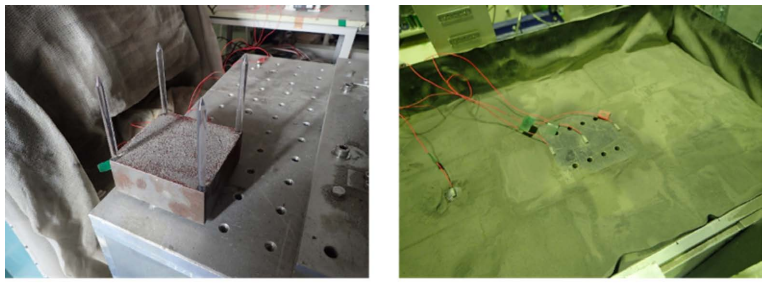

Figure 5. Photograph of specimen.

Table 1. Scaling law.

Item		1 g field	(1/6) g field
Length		1	6
Time		1	6
Acceleration		1	1/6
Regolith	Strain	1	1
	Stress	1	1
Frequency		1	1/6

Table 2. Maximum input acceleration.

Input wave	Maximum input acceleration (cm/s²)	
	1 g field	(1/6) g field
Wave1	36	5.9
Wave2	62	10.3
Wave3	131	21.9
Wave4	252	42.0
Wave5	372	61.9

2. Triaxial Compression Test of Regolith Simulant

2.1. Test Conditions

Static (consolidated drained) and cyclic triaxial compression tests were performed on the regolith simulant. These tests were conducted in accordance with JGS standards [17]. For each test, three specimens were prepared at relative densities of D_r = 60% and 80%. To render the specimens free-standing, water was added, they were frozen, placed in the testing machine, thawed, and then subjected to testing. The static triaxial compression tests were carried out under a back pressure of 100 kN/m^2 and with confining pressures σ'_3 set at 30, 60, and 120 kN/m^2. Meanwhile, the cyclic triaxial compression tests were conducted under a back pressure of 100 kN/m^2 and a confining pressure of σ'_3 = 50 kN/m^2, with loading frequencies f set at 0.5, 1.0, and 2.0 Hz.

2.2. Static Triaxial Compression Test Results

Figure 6 displays photographs captured before and after the test, while Figure 7 illustrates the axial stress–axial strain and volumetric strain–axial strain relationships. In Figure 7(a), it is evident that under identical relative densities, higher confining pressures yield greater initial stiffness and maximum stress. Conversely, at the same confining pressure, specimens with a relative density of 80% exhibit higher maximum stress initially, followed by a notable decline in yield strength. Figure 7(b) further reveals that the specimen experiences contraction during the initial loading stage, progressing to expansion with increased axial strain. This volumetric change is more prominent in specimens with higher relative density and lower confining pressure.

Figure 8 demonstrates the internal friction angle and cohesion, crucial parameters within the Mohr-Coulomb model. The internal friction angle notably reaches approximately 45˚ for the specimen with a relative density of 80%. Additionally, the cohesion measures approximately 8 kN/m^2 for the specimen with a relative density of 80%.

2.3. Cyclic Triaxial Compression Test Results

Figure 9 presents a comparison between the shear stiffness ratio concerning the initial shear stiffness G/G_0 and shear strain γ, alongside the equivalent damping

(a) Before test (b) After test

Figure 6. Specimen of static triaxial compression test (D_r = 80%).

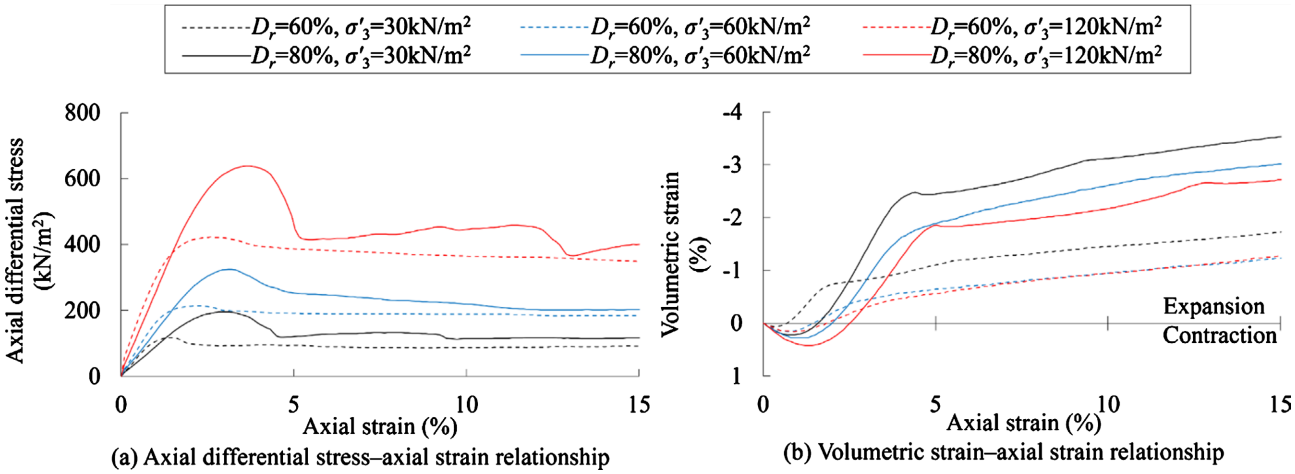

(a) Axial differential stress–axial strain relationship (b) Volumetric strain–axial strain relationship

Figure 7. Static triaxial compression test results.

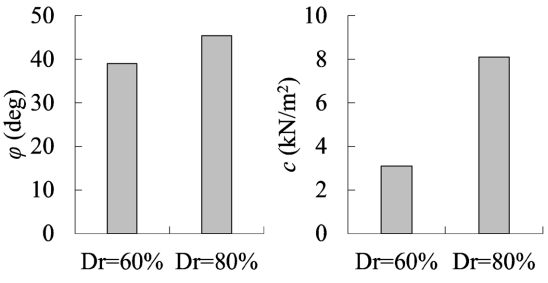

(a) Internal friction angle φ (b) Cohesion c

Figure 8. Mohr-Coulomb model parameters from test results.

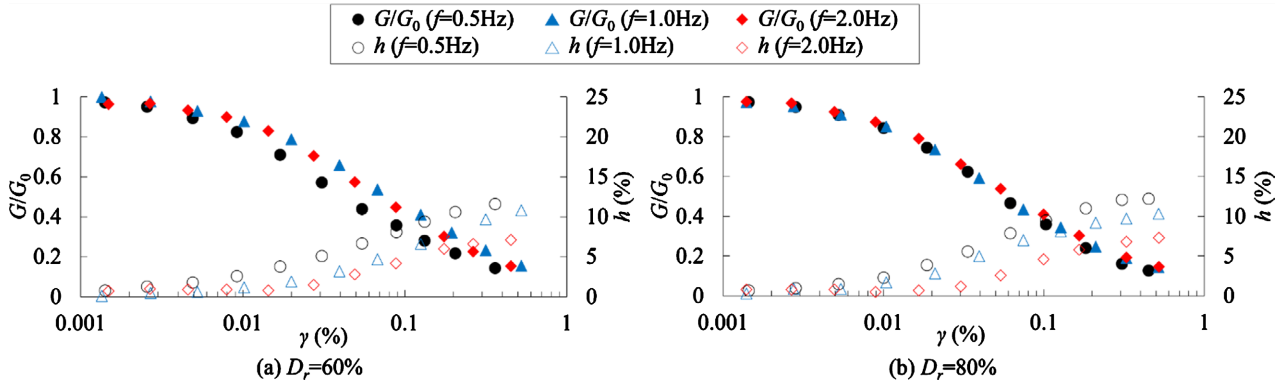

(a) D_r=60% (b) D_r=80%

Figure 9. Dynamic deformation characteristics (comparison by loading frequency).

factor *h* and shear strain (depicting "dynamic deformation characteristics") across varying loading frequencies. At a relative density of 60%, the shear stiffness ratio appears slightly lower during 0.5 Hz loading, but notable differences between both relative densities are absent even with diverse loading frequencies. Meanwhile, the equivalent damping factor diminishes as the loading frequency rises for both relative densities.

Figure 10 compares dynamic deformation characteristics based on relative density. Minimal differences were observed between relative densities for both the shear stiffness ratio and equivalent damping factor.

Figure 11 illustrates the dynamic deformation characteristics of the regolith simulant in comparison with sandy and clayey soils on Earth. This study utilizes Koyamada *et al.*'s model [18] for Earthly soils, averaging dynamic deformation characteristics from ground samples sourced from Tokyo, Kanagawa, and Osaka. Notably, the shear stiffness ratio of regolith simulant decreases earlier than that of the sandy soil in Reference [18] as shear strain increases. Additionally, while variations occur based on loading frequency, the equivalent damping factor of the regolith simulant tends to be lower than that of the sandy soil in Reference [18].

Figure 12 represents the strain at which the secant stiffness is half of the initial

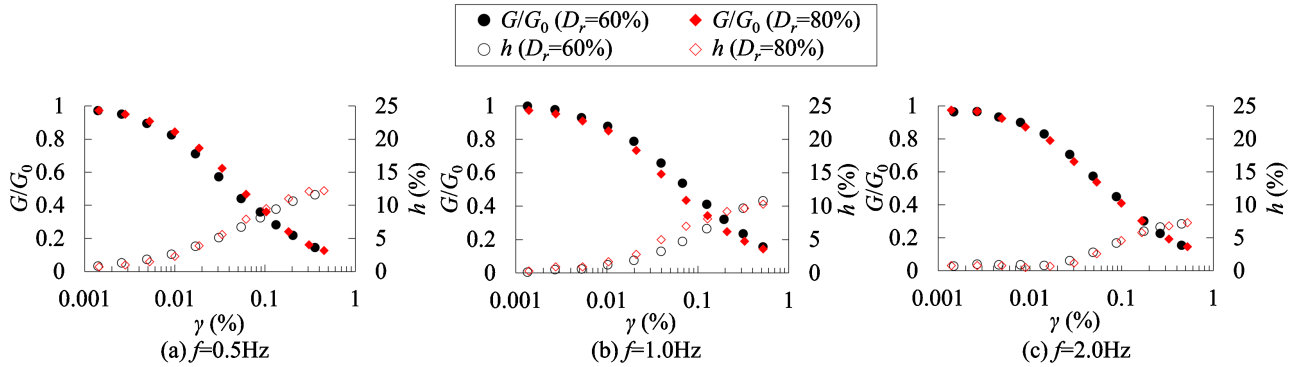

Figure 10. Dynamic deformation characteristics (comparison by relative density).

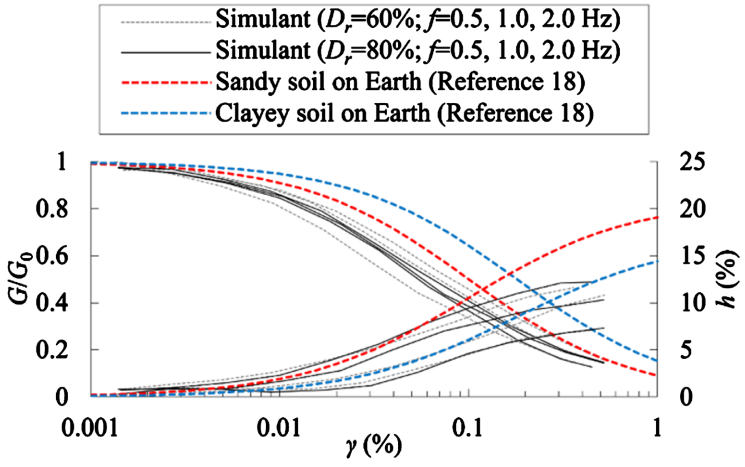

Figure 11. Comparison of Earth soil and simulant.

stiffness, called the reference strain, and maximum damping factor when fitting the dynamic deformation characteristics in Figure 9 and Figure 10 to the Hardin-Drnevich model. The reference strain of the regolith simulant is lower than 0.10%, contrasting with the value for sandy soil in Reference [18]. Moreover, the maximum damping factor of the regolith simulant is less than 15% for all specimens, decreasing with rising loading frequencies.

3. Regolith Simulant Shaking Table Test

The shaking table test results are displayed for scenarios involving solely the regolith ground, as well as the direct foundation, buried foundation, and pile foundation installed on the regolith ground. Time and frequency in the experimental outcomes are expressed according to a model scale (1 g field).

3.1. Free Ground Response

Figure 13 illustrates a comparison of the Fourier amplitude ratio depicting the ground's response to the input (shaking table acceleration) of Waves 1 and 5 at various depths. A clear amplification of shaking within the ground can be observed for both inputs.

Figure 14 showcases a comparison of the Fourier amplitude ratios representing the ground's response concerning the input amplitude of Waves 1 - 5. As the input increased, the ground exhibited a decrease in its dominant frequency

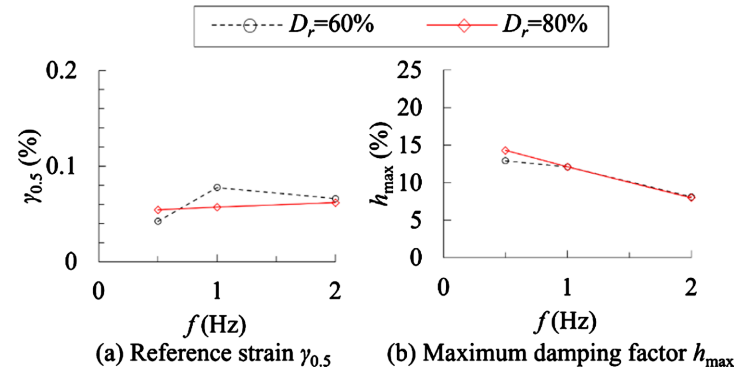

Figure 12. Hardin-Drnevich model parameters from test results.

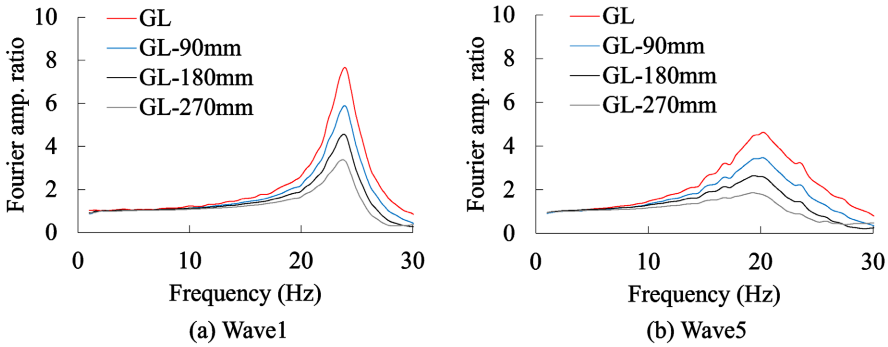

Figure 13. Fourier amplitude ratio of ground response with respect to input (comparison by depth).

from approximately 23 Hz to approximately 20 Hz, accompanied by a reduction in the amplification factor. This emphasized the significant nonlinearity inherent in the regolith ground.

3.2. Specimen Response

3.2.1. Maximum Response Acceleration and Response Waveform

Figure 15(a) depicts the relationship between the maximum horizontal acceleration and input acceleration at the top of the structure. Notably, no distinct variance was observed in the maximum response values between the direct foundation and the buried foundation. Conversely, the pile foundation exhibited a greater acceleration response compared to the other specimens.

Figure 15(b) illustrates the relationship between the maximum horizontal acceleration caused by the rocking component of the horizontal acceleration at the top of the specimen and the input acceleration. Here, the calculated acceleration, derived by multiplying the angular acceleration (obtained from the vertical acceleration measured at both ends of the specimen) by the height of the structure, represents the horizontal response attributed to the rocking component. Comparative analysis indicates a considerable suppression of the horizontal response attributed to the rocking component in both the buried foundation and pile foundation, in contrast to the scenario involving a non-buried direct foundation. This suppression suggests that the regolith ground on the side of the specimen played a resisting role in the buried foundation, while in the pile foundation, the regolith ground around the pile's tip and its surrounding surface acted as the resisting factors.

Figure 16 exhibits time history waveforms of horizontal acceleration at the top of the structure for both the direct foundation and pile foundation during maximum vibration (Wave 5). Additionally, Figure 16(c) illustrates the response waveform of the pile foundation during minimum vibration (Wave 1) for comparative analysis. Comparing the response waveform of the pile foundation during maximum vibration to that of the direct foundation during maximum vibration and the pile foundation during minimum vibration, it is evident that the former features a longer period and a distinct spike-like peak. For the pile

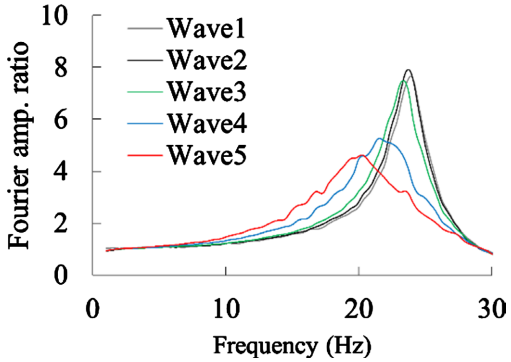

Figure 14. Fourier amplitude ratio of ground response with respect to input (comparison by input amplitude).

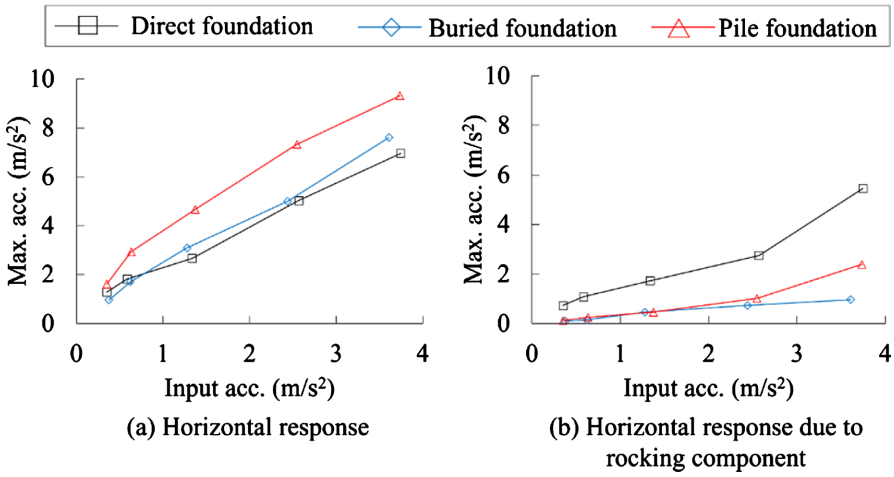

Figure 15. Maximum response acceleration at top of structure.

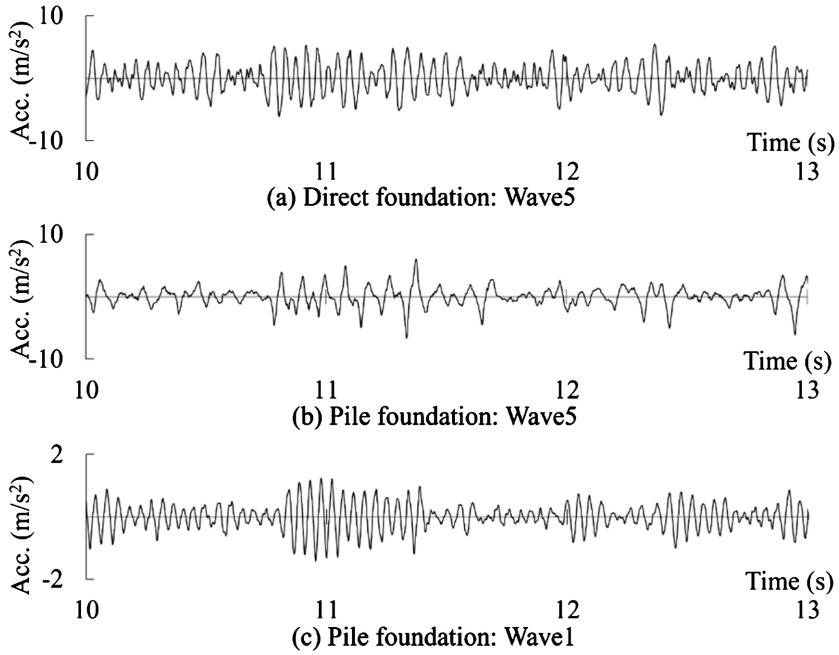

Figure 16. Acceleration waveform of horizontal response at top of structure.

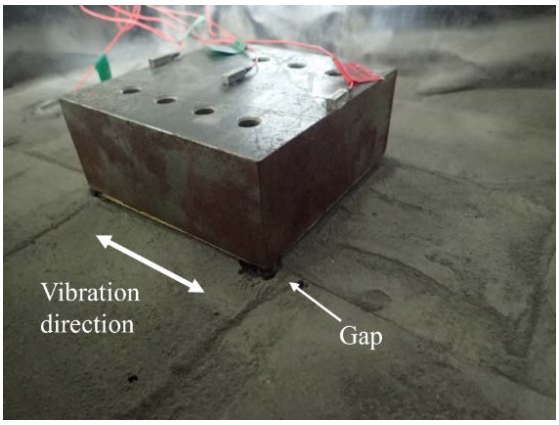

Figure 17. Pile foundation specimen after maximum vibration.

foundation, the boundary between rounded and spiked waveforms is between Waves 2 and 3.

Figure 17 displays a photograph of the pile foundation specimen after maximum vibration. A visible gap between the ground around the pile head suggests a separation phenomenon between the pile and the ground. This indicates the likelihood of the pile vibrating within the gap, causing significant peaks of acceleration upon contact with the ground. Moreover, the protruding pile head likely contributes to the increased horizontal response observed in the pile foundation.

3.2.2. Fourier Amplitude Ratio

Figure 18 presents the Fourier amplitude ratio of the horizontal response at the top of the structure with respect to the input, compared across different input amplitudes. Across all foundations, increased input amplitude correlated with a lower predominant frequency and generally smaller amplification factors, notably accentuating nonlinearity, especially evident in the pile foundation. The observed behavior in the pile foundation suggests that the response of the coupled system was influenced by nonlinearity arising from ground plasticization and separation around the piles.

Figure 19 illustrates the Fourier amplitude ratio of the horizontal response attributed to the rocking component at the top of the structure with respect to the input, comparing different input amplitudes. For the direct foundation, larger input amplitudes decreased the predominant frequency while amplification

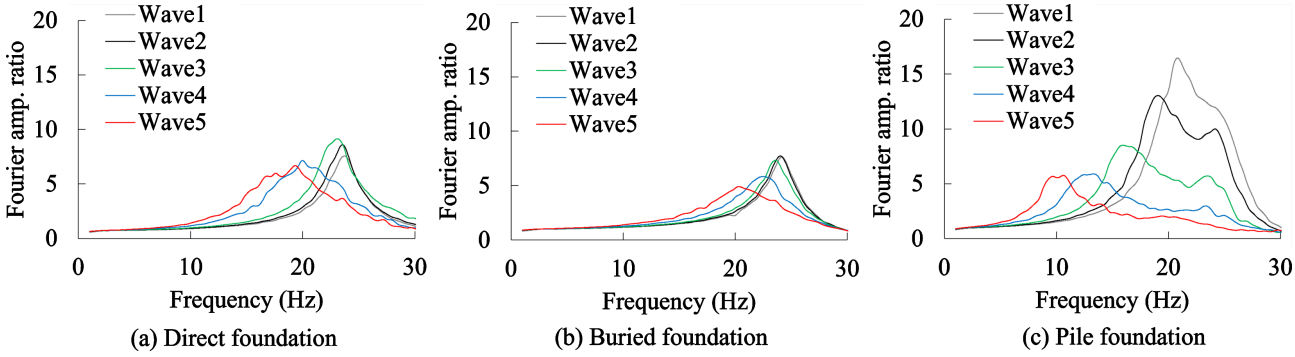

Figure 18. Fourier amplitude ratio of horizontal response at top of structure with respect to input.

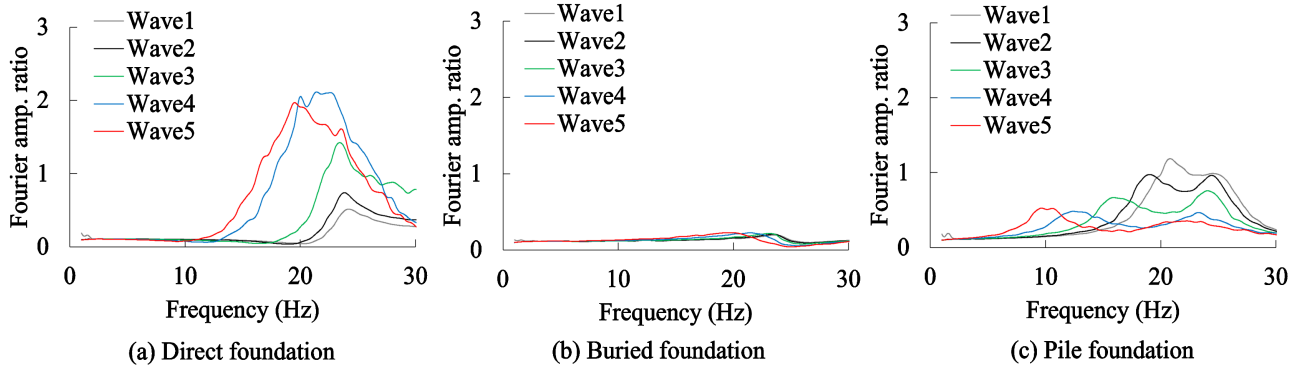

Figure 19. Fourier amplitude ratio of horizontal response due to rocking component at top of structure with respect to input.

factors increased. In contrast, the buried foundation showcased notably reduced response. Moreover, within the pile foundation, larger input amplitudes decreased the predominant frequency and decreased the amplification factor. At maximum vibration, the pile foundation's response was particularly suppressed when compared to that of the direct foundation.

These results indicate the effectiveness of pile foundations and buried foundations in suppressing the horizontal response attributed to the rocking component amid vibration disturbances, especially when constructing structures with a high tower ratio or a significant center of gravity, such as parabolic antennas.

4. Conclusions

In this study, we conducted regolith simulant soil tests and shaking table experiments, yielding fundamental insights into the response properties of lunar structures. The key findings of this study can be summarized as follows.

In static triaxial compression tests of the regolith simulant, the specimen with a relative density of 80% exhibited an internal friction angle of approximately 45˚. After reaching maximum stress, a decline in yield strength was observed. Meanwhile, cyclic triaxial compression tests demonstrated that the reference strain and equivalent damping factor of the regolith simulant were smaller compared to sandy soil on Earth.

Shaking table tests were performed on the direct foundation, buried foundation, and pile foundation installed on regolith ground. Similar to observations with sandy ground on Earth, increased input amplitude led to a nonlinear response from the regolith ground and each type of foundation. However, the buried foundation and pile foundation notably suppressed the horizontal response attributed to the rocking component compared to a direct foundation. Notably, the pile foundation displayed heightened nonlinearity in its horizontal response due to the pile head protrusion and the separation between the pile and ground, concurrently exhibiting increased acceleration response. These outcomes suggest similar response properties between lunar regolith and sandy ground on Earth. Nonetheless, further investigation is essential to explore the influence of regolith soil properties under low confining pressure and to delve into the response characteristics of structures and regolith ground in a lunar surface environment characterized by low gravity and vacuum conditions.

Conflicts of Interest

The authors declare no conflicts of interest regarding the publication of this paper.

References

[1] National Aeronautics and Space Administration, Lyndon B. Johnson Space Center (1975) Apollo Program Summary Report. National Aeronautics and Space Administration, Washington DC.

[2] National Aeronautics and Space Administration (2020) Artemis Plan—NASA's

Lunar Exploration Program Overview. National Aeronautics and Space Administration, Washington DC.

[3] Special Research Committee on Space Habitat, Architectural Institute of Japan (2023) Report of the Special Research Committee on Space Habitat. Architectural Institute of Japan, Tokyo. (In Japanese)

[4] Matsushima, T. and Kobayashi, T. (2021) Space Exploration and Geotechnical Engineering—Chapter 4—Mechanics of Planetary Regolith. *Geotechnical Engineering Magazine*, **69**, 43-51. (In Japanese)

[5] Kobayashi, T. and Fukagawa, R. (2021) Space Exploration and Geotechnical Engineering—Chapter 5—Space Explorations and Geotechnical Engineering. *Geotechnical Engineering Magazine*, **69**, 89-97. (In Japanese)

[6] Miyamoto, H., Tachibana, S., Hirata, N. and Sugita, S. (2008) Planetary Geology. University of Tokyo Press, Tokyo. (In Japanese)

[7] Heiken, G.H., Vaniman, D.T. and French, B.M. (1991) Lunar Source Book: A User's Guide to the Moon. Cambridge University Press, Cambridge.

[8] Ohtake, M., Saiki, K. and Miyamoto, H. (2021) Space Exploration and Geotechnical Engineering—Chapter 3—Formation of the Lunar and Planetary Surface. *Geotechnical Engineering Magazine*, **69**, 57-65. (In Japanese)

[9] Kanamori, H., Udagawa, S., Yoshida, T., Matsumoto, S. and Takagi, K. (1998) Properties of Lunar Soil Simulant Manufactured in Japan. *Space*, **98**, 462-468. https://doi.org/10.1061/40339(206)53

[10] Fujimura, A. (1991) Seismological Exploration on Extraterrestrial Bodies. *Journal of the Seismological Society of Japan*, 2*nd Series*, **44**, 41-51. (In Japanese) https://doi.org/10.4294/zisin1948.44.Supplement_41

[11] Lammelein, D.R., Latham, G.V., Dorman, J., Nakamura, Y. and Ewing, M. (1974) Lunar Seismicity, Structure, and Tectonics. *Reviews of Geophysics and Space Physics*, **12**, 1-21. https://doi.org/10.1029/RG012i001p00001

[12] Lammelein, D.R. (1977) Lunar Seismicity and Tectonics. *Physics of the Earth and Planetary Interiors*, **14**, 224-273. https://doi.org/10.1016/0031-9201(77)90175-3

[13] Goins, N.R., Dainty, A.M. and Toksöz, M.N. (1981) Lunar Seismology: The Internal Structure of the Moon. *Journal of Geophysical Research*, **86**, 5061-5074. https://doi.org/10.1029/JB086iB06p05061

[14] Nakamura, Y., Latham, G.V. and Dorman, H.J. (1982) Apollo Lunar Seismic Experiment—Final Summary. *Journal of Geophysical Research*, **87**, A117-A123. https://doi.org/10.1029/JB087iS01p0A117

[15] Araki, H. (1994) Elucidation of Moonquake Generation Patterns and Application to Moonquake Observations in LUNAR-A Project. Ph.D. Thesis, The University of Tokyo, Tokyo. (In Japanese)

[16] Miyamoto, Y., Miura, K., Scott, R.F. and Hushmand, B. (1992) Pile Foundation Response in Liquefiable Soil Deposit during Strong Earthquakes. *Journal of Structural and Construction Engineering* (*Transactions of AIJ*), No. 439, 49-63. https://doi.org/10.3130/aijsx.439.0_49

[17] The Japanese Geotechnical Society (2020) Japanese Standards and Explanations of Laboratory Tests of Geomaterials (The First Revised Edition). The Japanese Geotechnical Society, Tokyo. (In Japanese)

[18] Koyamada, K., Miyamoto, Y. and Miura, K. (2003) Nonlinear Property for Surface Strata from Natural Soil Samples. *Proceedings of the* 38*th Japan National Conference on Geotechnical Engineering*, Akita, 2-4 July 2003, 2077-2078. (In Japanese)